

# Co-VeGAN: Complex-Valued Generative Adversarial Network for Compressive Sensing MR Image Reconstruction

Bhavya Vasudeva<sup>1\*</sup>      Puneesh Deora<sup>1\*</sup>  
<sup>1</sup>Dept. of ECE, IIT Roorkee, India

Saumik Bhattacharya<sup>2</sup>      Pyari Mohan Pradhan<sup>1</sup>  
<sup>2</sup>Dept. of E&ECE, IIT Kharagpur, India

## Abstract

*Compressive sensing (CS) is widely used to reduce the image acquisition time of magnetic resonance imaging (MRI). Though CS based undersampling has numerous benefits, like high quality images with less motion artefacts, low storage requirement, etc., the reconstruction of the image from the CS-undersampled data is an ill-posed inverse problem which requires extensive computation and resources. In this paper, we propose a novel deep network that can process complex valued input to perform high-quality reconstruction. Our model is based on generative adversarial network (GAN) that uses residual-in-residual dense blocks in a modified U-net generator with patch based discriminator. We introduce a wavelet based loss in the complex GAN model for better reconstruction quality. Extensive analyses on different datasets demonstrate that the proposed model significantly outperforms the existing CS reconstruction techniques in terms of peak signal-to-noise ratio and structural similarity index.*

## 1. Introduction

Magnetic resonance imaging (MRI) is a frequently used medical imaging modality in clinical practice as it proves to be an excellent non-invasive source for revealing structural as well as anatomical information. A major shortcoming of the MRI acquisition process is its considerably long scan time. This is due to sequential acquisition of large volumes of data, not in the image domain but in k-space, i.e. Fourier domain. Such a prolonged scanning time can cause significant artefacts because of physiological motion, movement of patient during the scan. It may also hinder the use of MRI in time-critical diagnosis.

A possible way to speed up the imaging process is by parallel imaging techniques [30], [11]. However, the number and arrangement of the receiver coils severely impact the acceleration factor for such techniques, and could possibly introduce imaging artefacts. Another possible way

for fast acquisition is leveraging compressive sensing (CS) [8] theory based undersampling, which is used very often for this purpose. However, doing this renders the inverse problem ill-posed, making the recovery of high-quality MR images extremely challenging. Moreover, the presence of noise during the acquisition may also severely impact the reconstruction quality.

Conventional approaches for CS-MRI reconstruction focus extensively on the usage of sparse representations to assume prior knowledge on the structure of the MR image to be reconstructed. Sparse representations can be explored by the use of predefined transforms [24] such as total variation, discrete cosine transform, discrete wavelet transform, discrete Fourier transform, etc. Alternatively, dictionary learning based methods [32] learn sparse representations from the subspace spanned by the data. Both these types of approaches suffer from long computation time due to the iterative nature of the optimization processes. Moreover, the universally applicable sparsifying transforms might find it difficult to completely capture the fine details as observed in biological tissues [23].

Deep learning frameworks have enjoyed great success in similar inverse problems such as single-image super resolution [7], denoising [39], etc., where the methods try to recover missing information from incomplete/ noisy data. Yang *et al.* [41] used the alternating direction method of multipliers (ADMM) algorithm [4] to train their deep network for CS-MRI reconstruction. With the recent advancements of generative adversarial networks (GANs) [10, 18], CS-MRI reconstruction problems are also addressed using adversarial learning framework. In a recent study, Bora *et al.* [3] have shown that pretrained generative models like variational autoencoders and GANs [10] can be used for recovery of CS signal without making use of sparsity at all. Yang *et al.* [40] proposed a U-net [34] based generator, following a refinement learning based approach, with mean square error (MSE) and perceptual loss to reconstruct the images. In [31], authors proposed fully residual network using addition-based skip connections. They used cyclic loss for data consistency constraints in the training process to achieve better reconstruction quality. Deora *et al.* [6]

\*equal contribution

proposed a U-net based generator with patch discriminator [18] based model to perform the reconstruction task. Along with mean absolute error (MAE) and structural similarity (SSIM) [42], authors used Wasserstein loss [1] to improve the adversarial learning. Mardani *et al.* [25] introduced affine projection operator in-between the generator and the discriminator to improve the data consistency in the reconstructed images. Though deep adversarial networks have significantly improved the quality of the CS-MRI reconstruction, one of the biggest short-comings is that they work on real-valued inputs though the input is inherently complex-valued. The other limitation is that almost all reconstruction networks depend on pixel-based  $l_2$  or  $l_1$  losses. This efficiently reconstructs the low frequency components of data, but often fails to generate the middle and high frequency information which depicts fine textural and contextual parts of an image [16].

*Motivation of the work:* Complex parameter space provides several benefits over real parameter space. Apart from having biological inspiration and significance [33], complex-valued representation not only increases the representational capacity of the network, it can be more stable than real-valued space in various applications [36, 5]. Complex-valued operations can be performed with easy optimization techniques [27] without sacrificing the generalization ability of the network [14]. Several researchers have reported that the complex-valued neural network exhibits faster learning with better robustness to noise [5, 2, 38]. Complex-valued operations also preserve the phase information which encodes fine structural details of an image [36, 28]. Even with these striking benefits, complex-valued deep networks are not widely explored. In fact, to the best of our knowledge, complex-valued GAN (Co-VeGAN) model has never been explored for any reconstruction problem.

*Contributions:* The contributions of this work are as follows.

- Complex-valued operations are widely unexplored for GAN architecture, and it has never been explored for CS-MRI reconstruction problem. This work not only exploits complex-valued operations to achieve better reconstruction, but also documents the stability and quality of a Co-VeGAN approach for a reconstruction problem with various losses like  $l_1$ , SSIM, etc.
- We have proposed a novel generator architecture by modifying the existing U-net model [34].
- As CS-MRI problem formulation is closely related to super-resolution problems, taking an inspiration from [16], we introduce wavelet loss in our model to better reconstruct mid-frequency components of the MR image. To the best of our knowledge, wavelet loss has

never been integrated with any complex-valued neural network before.

## 2. Methodology

The acquisition model of MRI can be described as follows:

$$\mathbf{y} = \Phi \mathbf{X} + \zeta = \mathbf{U} \text{vec}(\mathbf{F} \mathbf{X}) + \zeta \quad (1)$$

where  $\mathbf{X} \in \mathbb{R}^{K \times K}$  is the desired image,  $\mathbf{y} \in \mathbb{C}^{M \times 1}$  denotes the observed data vector, the vector  $\zeta \in \mathbb{C}^{M \times 1}$  captures the noise.  $\mathbf{F}$  denotes the matrix to compute the 2D Fourier transform,  $\mathbf{U} \in \mathbb{R}^{M \times K^2}$  describes the matrix for undersampling, and  $\text{vec}(\cdot)$  denotes vectorization. Given an observation  $\mathbf{y}$ , the aim of reconstruction is to recover  $\mathbf{X}$  in the presence of a non-zero noise vector  $\zeta$ . We attempt the recovery of  $\mathbf{X}$  by using a GAN model.

### 2.1. Complex-valued GAN

A GAN comprises of two networks, namely a generator  $G$  and a discriminator  $D$ . In order to generate images which are similar to the samples of the distribution of true data  $\mathbf{y}_t$ , the generator attempts to map an input vector  $\mathbf{z}$  to the output  $G(\mathbf{z})$ . On the other hand, the discriminator aims to classify the generated samples  $G(\mathbf{z})$  and the samples from the distribution of  $\mathbf{y}_t$ .

We propose the use of a complex-valued GAN, where the generator  $G : \mathbb{C}^{K \times K} \rightarrow \mathbb{R}^{K \times K}$ , and the discriminator  $D : \mathbb{R}^{K \times K} \rightarrow \mathbb{R}^{1 \times 1}$  can be complex-valued networks. However, since both the generated and ground truth (GT) images are real-valued, we stick to the use of a real-valued discriminator.

### 2.2. Complex-valued operations

In this section, we discuss the important operations required for the implementation of a complex-valued network, namely convolution, backpropagation, batch normalization (BN) [17], and activation.

The complex-valued equivalent of real-valued 2D convolution is discussed below. The convolution of a complex-valued kernel  $\mathbf{W} = \mathbf{W}_R + i\mathbf{W}_I$  with complex-valued feature maps  $\mathbf{F} = \mathbf{F}_R + i\mathbf{F}_I$ , can be represented as  $\mathbf{A} = \mathbf{W} * \mathbf{F} = \mathbf{A}_R + i\mathbf{A}_I$ , where

$$\begin{aligned} \mathbf{A}_R &= \mathbf{W}_R * \mathbf{F}_R - \mathbf{W}_I * \mathbf{F}_I \\ \mathbf{A}_I &= \mathbf{W}_R * \mathbf{F}_I + \mathbf{W}_I * \mathbf{F}_R \end{aligned} \quad (2)$$

In these notations, subscripts **R** and **I** denote the real and imaginary parts, respectively. In order to implement the aforementioned complex-valued convolution, we use real-valued tensors, where  $\mathbf{W}$  ( $\mathbf{F}$ ) is stored such that the imaginary part  $\mathbf{W}_I$  ( $\mathbf{F}_I$ ) is concatenated to the real part  $\mathbf{W}_R$  ( $\mathbf{F}_R$ ). The resultant includes four real-valued 2D convolutions as mentioned in (2), which is stored in a similar manner by concatenating  $\mathbf{A}_I$  to  $\mathbf{A}_R$ .

Backpropagation can be performed on a function  $f$  that is non-holomorphic as long as it is differentiable with respect to its real and imaginary parts [21]. Since all the loss functions considered in this work are real-valued, we consider  $f$  to be a real-valued function of weight vector  $\mathbf{w}$ . The update rule of  $\mathbf{w}$  using gradient descent can be written as:

$$\mathbf{w} = \mathbf{w} - \rho \nabla_{\bar{\mathbf{w}}} f(\mathbf{w}) \quad (3)$$

where  $\rho$  is the learning rate,  $\bar{\mathbf{w}}$  denotes the complex conjugate, and the gradient of  $f$  is calculated as follows:

$$\begin{aligned} \nabla_{\bar{\mathbf{w}}} f(\mathbf{w}) &= \left[ \frac{\partial f}{\partial \bar{w}_1} \cdots \frac{\partial f}{\partial \bar{w}_n} \right]^T \\ \frac{\partial f}{\partial \bar{w}} &= \frac{1}{2} \left( \frac{\partial f}{\partial w_R} + i \frac{\partial f}{\partial w_I} \right) \end{aligned} \quad (4)$$

We make use of the complex BN applicable to complex numbers, proposed by [36]. To ensure that the complex data is scaled in such a way that the distribution of real and imaginary components is circular, the 2D complex vector can be whitened as follows:

$$\mathbf{x}_{std} = \mathbf{B}^{-\frac{1}{2}} (\mathbf{x} - \mathbb{E}[\mathbf{x}]) \quad (5)$$

where  $\mathbf{B}$  denotes the covariance matrix, and  $\mathbb{E}$  denotes expectation operator. It can be represented as:

$$\mathbf{B} = \begin{bmatrix} \text{Cov}(\mathbf{x}_R, \mathbf{x}_R) & \text{Cov}(\mathbf{x}_R, \mathbf{x}_I) \\ \text{Cov}(\mathbf{x}_I, \mathbf{x}_R) & \text{Cov}(\mathbf{x}_I, \mathbf{x}_I) \end{bmatrix} \quad (6)$$

Learnable parameters  $\gamma, \beta$  are used to scale and shift the aforementioned standardized vector as follows:

$$\mathbf{x}_{BN} = \gamma \mathbf{x}_{std} + \beta \quad (7)$$

where  $\gamma$  is a  $2 \times 2$  matrix, and  $\beta$  is a complex number.

In order to work with complex-valued entities, several activations have been proposed in previous works [2]. In this work, the following complex-valued activations are considered:

1. Complex rectified linear unit (CReLU): The complex equivalent of ReLU, known as CReLU, is obtained when ReLU is applied separately to the real and imaginary parts of an element. It is formulated as follows:

$$\text{CReLU}(a) = \text{ReLU}(a_R) + i\text{ReLU}(a_I) \quad (8)$$

where  $a$  is a complex-valued input.

2. Complex parametric ReLU (CPReLU): The complex equivalent of PReLU [13] is obtained when PReLU is applied separately to the real and imaginary parts of an element. The expression for CPReLU is given by:

$$\text{CPReLU}(a) = \begin{cases} a_R + ia_I & a_R \geq 0, a_I \geq 0 \\ \beta_R a_R + ia_I & a_R < 0, a_I \geq 0 \\ a_R + i\beta_I a_I & a_R \geq 0, a_I < 0 \\ \beta_R a_R + i\beta_I a_I & a_R < 0, a_I < 0 \end{cases}$$

where  $\beta_R$  and  $\beta_I$  are trainable parameters.

3. *zReLU* [12]: This activation allows a complex element to pass only if both its real and imaginary parts are positive. It is given by:

$$zReLU(a) = \begin{cases} a_R + ia_I & a_R \geq 0, a_I \geq 0 \\ 0 & \text{otherwise} \end{cases} \quad (9)$$

## 2.3. Network Architecture

The generator architecture of the proposed model is shown in Fig. 1. It is based on a U-net architecture. The left side is a contracting path, where each step involves the creation of downsampled feature maps using a convolutional layer with a stride of two, which is followed by BN and activation. The right side is an expanding path, where each step consists of upsampling (by a factor of two), convolutional layer to create new feature maps, followed by BN and activation layers.

In order to provide richer context about the low-level features for superior reconstruction, the low-level feature maps from the contracting path are concatenated to the high-level feature maps of same size in the expanding path. In this work, we propose the use of dense connections between the steps (layers) within the contracting as well as the expanding path. These dense connections [15] help to improve the flow of information between the layers and encourage the features to be reused from the preceding layers. There is also an added benefit of increase in variation of available information by concatenation of feature maps. Since the feature maps at various layers are not of the same size, the average pooling and upsampling (with bilinear interpolation) operations have been introduced in the connections between the layers of the contracting path and the expanding path, respectively. However, the use of these operations to change the size of the feature maps by a factor greater than  $r$  (less than  $K/2^r \times K/2^r$ ) not only increases the computational and memory requirement, but also reduces the quality of information available to the subsequent layers. As shown in Fig. 1, the parameter  $r$  is set as 3 in this work.

Further, residual-in-residual dense blocks (RRDBs) [37] are incorporated at the lowest layer of the generator, where feature maps of size  $K/32 \times K/32$  are present. Each block uses residual learning across each dense block, as well as across a group of three dense blocks. At both the levels, residual scaling is used, i.e. the residuals are scaled by  $\alpha$  before they are added to the identity mapping, as shown in Fig. 1. These RRDBs not only make the network length variable, because of the residual connections which make identity mappings easier to learn, but also make a rich amount of information accessible to the deeper layers, through the dense connections.

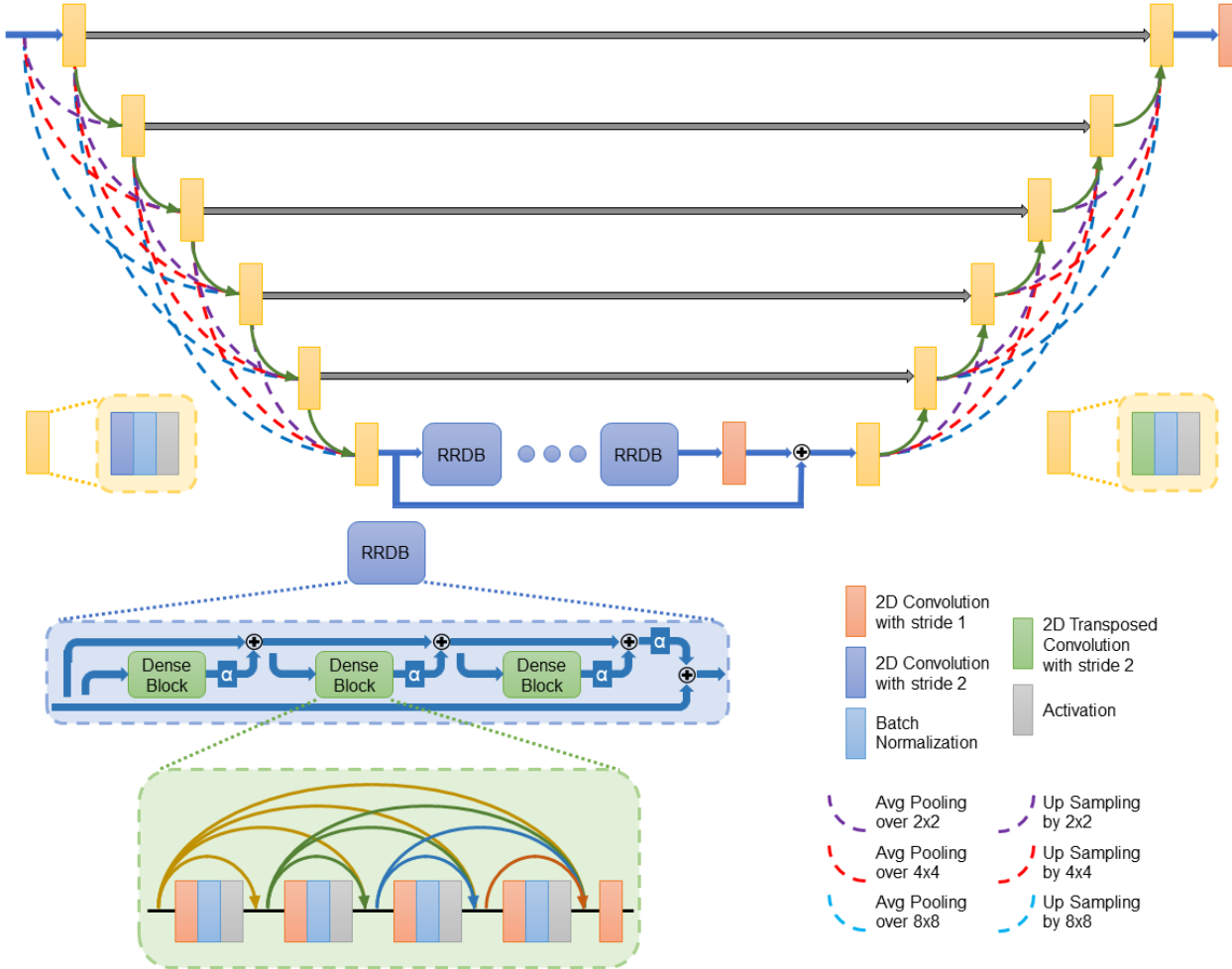


Figure 1. Generator architecture.

At the output of the generator, a hyperbolic tangent activation is applied, which brings the real as well as imaginary parts of the final feature map in the range  $[-1, 1]$ . These are brought to the range  $[0, 1]$ . In order to make the output real-valued, the absolute value is obtained (which lies in the range  $[0, \sqrt{2}]$ ), and then brought back to the range  $[-1, 1]$ .

The discriminator architecture is based on a standard convolutional neural network. It has 11 convolutional layers, each of which is followed by BN and activation. We use a patch based discriminator to increase the focus on the reconstruction of high frequency content. The patch based discriminator scores each patch of the image separately, and its output is the mean of the individual patch scores. This framework makes the network insensitive to the input size.

## 2.4. Training Losses

### 2.4.1 Adversarial Loss

In order to constrain the generator to produce the MR image corresponding to the samples acquired in the k-space, it is

conditioned [26] over the zero-filled reconstruction (ZFR) given by:

$$\mathbf{X}_u = \Phi^H \mathbf{y} = \mathbf{F}^H \text{mat}(\mathbf{U}^H \mathbf{y}) \quad (10)$$

where  $\mathbf{X}_u \in \mathbb{C}^{K \times K}$ ,  $H$  denotes the Hermitian operator, and  $\text{mat}(\cdot)$  denotes the conversion of vector to a square matrix. Conventionally, the solution to the minmax game between the generator and the discriminator is obtained by using binary cross-entropy based loss. However, it causes the problem of vanishing and exploding gradients, which makes the training of the GAN model unstable. In order to prevent this, Wasserstein distance based loss [1] is used. Mathematically, the training process of this conditional GAN using Wasserstein loss is formulated as follows:

$$\min_G \max_D L_{GAN} = \mathbb{E}_{\mathbf{X} \sim p_X(\mathbf{X})} [D(\mathbf{X})] - \mathbb{E}_{\mathbf{X}_u \sim p_{X_u}(\mathbf{X}_u)} [D(G(\mathbf{X}_u))] \quad (11)$$

where  $p_X(\mathbf{X})$  is the distribution of the GT images, and  $p_{X_u}(\mathbf{X}_u)$  is the distribution of the aliased ZFR images.

## 2.4.2 Content Loss

Besides adversarial loss, other losses are required to bring the reconstructed output closer to the corresponding GT image. In order to do so, we incorporate an MAE based loss, so that the pixel-wise difference between the GT and the generated image is minimized. It is given by:

$$L_{L_1} = \mathbb{E}[\|vec(G(\mathbf{X}_u) - \mathbf{X})\|_1] \quad (12)$$

where  $vec(\cdot)$  denotes vectorization, and  $\|\cdot\|_1$  denotes the  $\ell_1$  norm.

## 2.4.3 Structural Similarity Loss

As the high frequency details in the MR image help in distinguishing various regions of the brain, it is extremely important to improve their reconstruction. SSIM quantifies the similarity between the local patches of two images on the basis of luminance, contrast and structure. It is calculated as follows:

$$SSIM(\mathbf{M}, \mathbf{N}) = \frac{2\mu_M\mu_N + \epsilon_1}{\mu_M^2 + \mu_N^2 + \epsilon_1} \frac{2\sigma_{MN} + \epsilon_2}{\sigma_M^2 + \sigma_N^2 + \epsilon_2} \quad (13)$$

where  $\mathbf{M}$  and  $\mathbf{N}$  represent two patches of size  $K_p \times K_p$  from an image,  $\mu_M$  and  $\sigma_M^2$  denote the mean and variance of  $\mathbf{M}$ ,  $\mu_N$  and  $\sigma_N^2$  denote the mean and variance of  $\mathbf{N}$ , and  $\sigma_{MN}$  denotes the covariance of  $\mathbf{M}$  and  $\mathbf{N}$ .  $\epsilon_1$  and  $\epsilon_2$  are slack values to avoid division by zero.

In order to improve the perceptual quality of the reconstructed MR image and preserve the structural details, a mean SSIM (mSSIM) based loss is incorporated in the training of the generator. It maximizes the patch-wise SSIM between the generated image and the corresponding GT image, as follows:

$$L_{mSSIM} = 1 - \mathbb{E} \left[ \frac{1}{P} \sum_{p=1}^P SSIM(G_p(\mathbf{X}_u), \mathbf{X}_p) \right] \quad (14)$$

where  $P$  is the number of patches in the image.

## 2.4.4 Wavelet Loss

In order to further enhance the textural details in the generated image, a weighted version of MAE in the wavelet domain is included as another loss term. In order to decompose the image into sets of wavelet coefficients  $\mathbf{C}$ , which are equal in size, and correspond to even division of bands in the frequency domain, the wavelet packet transform is used. Fig. 2 depicts one step of the recursive process which is followed to obtain the sets of wavelet coefficients. For an  $r_w$  level decomposition which produces  $P_w = 4^{r_w}$  sets of wavelet coefficients of size  $K_w \times K_w$  with  $K_w = K/\sqrt{P_w}$ , the wavelet loss is formulated as follows:

$$L_{wt} = \frac{1}{P_w K_w^2} \sum_{p=1}^{P_w} \gamma_p \left[ \sum_{i=1}^{K_w} \sum_{j=1}^{K_w} |\mathbf{C}_{G(\mathbf{X}_u)}^p(i, j) - \mathbf{C}_{\mathbf{X}}^p(i, j)| \right]$$

where  $\gamma_p$  denotes the weight of the  $p^{th}$  set of coefficients. Since the pixel-wise MAE loss contributes more towards the improvement of low frequency details, and the mSSIM loss focuses more on preserving the high frequency content in the reconstructed image, higher weights  $\gamma_p$  are assigned to the wavelet coefficients corresponding to the band-pass components to improve their reconstruction. This is done by setting the weights according to the probability density function of a Gaussian distribution with mean  $(P_w - 1)/2$  and variance  $\sigma_w^2$ . In this work,  $r_w = 3$ , i.e.  $P_w = 64$ , and  $\sigma_w^2 = 12.5$ .

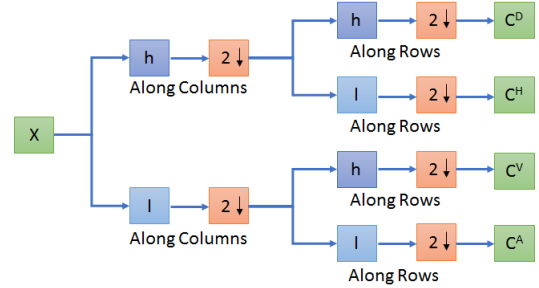


Figure 2. Illustration of the recursive process followed to compute the wavelet packet decomposition of  $\mathbf{X}$ . In this work, Haar wavelet is used, so that  $h = (1/\sqrt{2}, 1/\sqrt{2})$  and  $l = (1/\sqrt{2}, -1/\sqrt{2})$ .

## 2.4.5 Overall Loss

The overall loss  $L$  which is used to train the generator, is formulated as a weighted sum of the losses presented above:

$$L = \lambda_1 L_{GAN} + \lambda_2 L_{L_1} + \lambda_3 L_{mSSIM} + \lambda_4 L_{wt} \quad (15)$$

In this work,  $\lambda_1 = 0.01$ ,  $\lambda_2 = 20$ ,  $\lambda_3 = 1$ , and  $\lambda_4 = 100$ .

## 2.5. Training settings

For implementing the model, Keras framework with TensorFlow backend is used. The model is trained using 4 NVIDIA GeForce GTX 1080 Ti GPUs. In this work, the batch size is set as 16. In the generator, each layer produces 32 feature maps. The growth rate for the dense blocks in the RRDBs is set as 8,  $\alpha$  is 0.2, and 4 RRDBs are used. The absolute value of the discriminator weights is clipped at 0.05. For each generator update, the discriminator is updated thrice. For training the model, we use Adam optimizer [20], with  $\beta_1 = 0.5$  and  $\beta_2 = 0.999$ . The initial learning rate is set as  $10^{-4}$ , with a decay of  $1.39 \times 10^{-3}$ , so that it becomes  $1/10^{th}$  of the initial value after 5 epochs.

Table 1. Quantitative results for ablation study of the proposed model

Network Settings	1 <sup>st</sup>	2 <sup>nd</sup>	3 <sup>rd</sup>	4 <sup>th</sup>	5 <sup>th</sup>
Complex-valued GAN	✗	✓	✓	✓	✓
RRDBs	✗	✗	✓	✓	✓
Dense U-net	✗	✗	✗	✓	✓
Wavelet loss	✗	✗	✗	✗	✓
No. of generator parameters	2M	1.2M	1.2M	1.5M	1.5M
PSNR (dB)/ mSSIM	39.640/ 0.9823	40.048/ 0.9866	41.418/ 0.9879	43.798/ 0.9902	45.044/ 0.9919

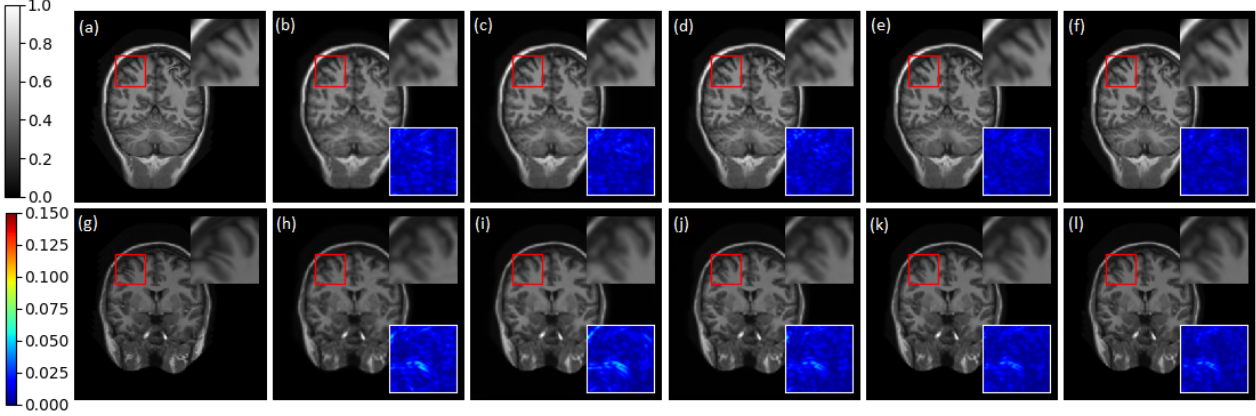


Figure 3. Qualitative results for ablation study of the proposed model. (a), (g) GT, reconstruction results for (b), (h) 1<sup>st</sup>, (c), (i) 2<sup>nd</sup>, (d), (j) 3<sup>rd</sup>, (e), (k) 4<sup>th</sup>, and (f), (l) 5<sup>th</sup> network settings. Inset- top right: the zoomed in region enclosed by the red box, bottom right: absolute difference between the zoomed in region and its corresponding GT.

### 3. Results and Discussion

We evaluate our models on T-1 weighted brain MR images from the MICCAI 2013 grand challenge dataset [22] as well as on T-2 weighted MR images of brain from the IXI dataset<sup>1</sup>.

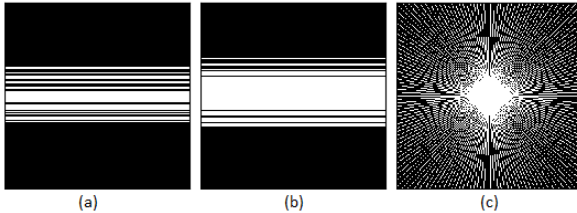


Figure 4. Undersampling masks used in this study. (a) 20% 1D Gaussian undersampling, (b) 30% 1D Gaussian undersampling, and (c) 30% radial undersampling.

For the MICCAI 2013 dataset, 20787 images are used for training, after randomly choosing images from the train set, and then applying data augmentation using images with 10% and 20% additive Gaussian noise. 1-D Gaussian undersampling is used in this case to generate 20% and 30% undersampled data using the masks shown in Fig. 4(a) and

(b), respectively. For testing, 2000 images are chosen randomly from the test set of the dataset. For the IXI dataset, 7500 images are randomly chosen for training and 100 non-overlapping images are chosen for testing. In this case, radial undersampling is used, with the mask shown in Fig. 4(c).

Table 2. Quantitative comparison of various activations

Activation	CReLU	zReLU	CPReLU
PSNR (dB)/ mSSIM	45.044/ 0.9919	35.9912/ 0.9690	45.377/ 0.9930

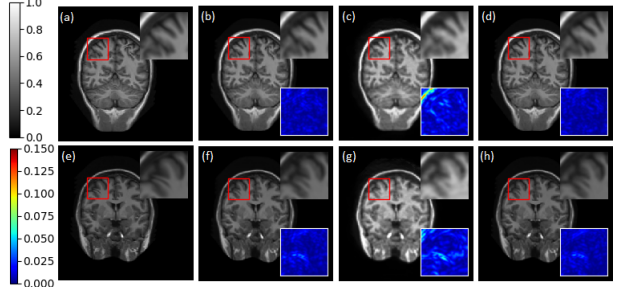


Figure 5. Qualitative comparison of various activations. (a), (e) GT, reconstruction results using (b), (f) CReLU, (c), (g) zReLU, (d), (h) CPReLU activations. Inset- top right: the zoomed in region enclosed by the red box, bottom right: absolute difference between the zoomed in region and its corresponding GT.

<sup>1</sup><https://brain-development.org/ixi-dataset/>

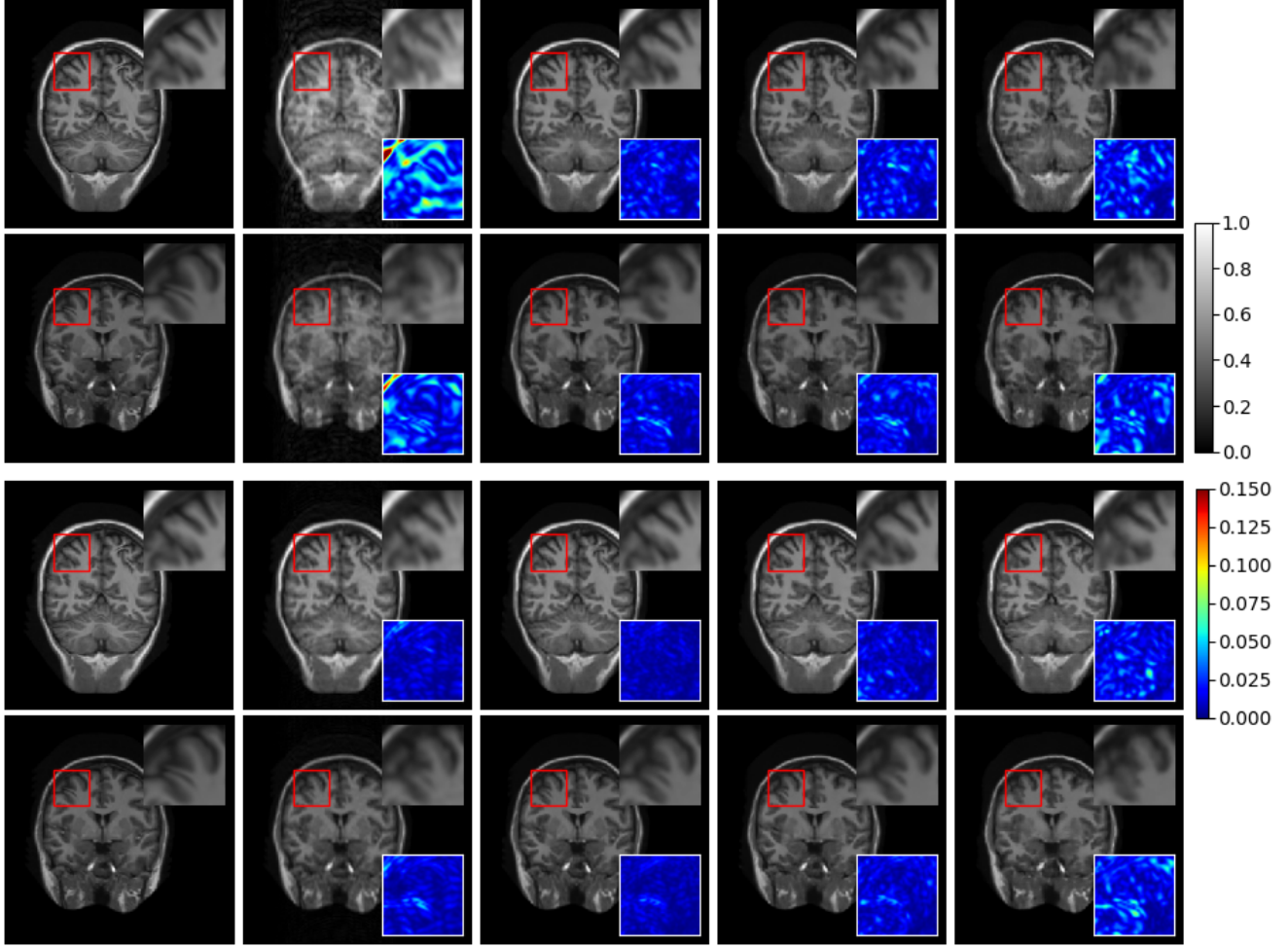


Figure 6. Qualitative results of the proposed model for two images. The first two rows show the reconstruction results for 20% undersampling. The last two rows show the reconstruction results for 30% undersampling. From left to right: GT, ZFR, reconstruction results for noise-free images, for images with 10% noise, and 20% noise. Inset- top right: the zoomed in region enclosed by the red box, bottom right: absolute difference between the zoomed in region and its corresponding GT.

Table 1 and Fig. 3 show the quantitative and qualitative results for ablation study of the model, respectively, to highlight the importance of various components used in the model. These results are reported for 30% undersampled images, from the MICCAI 2013 dataset. In the first case, a real-valued GAN model comprised of a U-net based generator without RRDBs, without the dense connections in the contracting and expanding paths, with ReLU activation and with  $\lambda_4 = 0$  in Eq. 15, is considered. In the next case, the complex-valued equivalent of the previous model is considered. In the third case, the effect of adding RRDBs in the last layer of the complex valued U-net is observed without the wavelet loss. In the fourth case, the addition of dense connections in the complex valued U-net is considered with the RRDBs, ignoring the wavelet loss. In the last case, the effect of including  $L_{wt}$  by setting  $\lambda_4 = 100$  is observed. Each step results in significant improvement in peak signal-

to-noise ratio (PSNR) as well as mSSIM. For the rest of the results, we use the network settings mentioned in the last stage.

Table 2 and Fig. 5 show the quantitative and qualitative results for comparing various activations, respectively. These results are also reported for 30% undersampled images, from the MICCAI 2013 dataset. It is observed that  $z$ ReLU has the worst, while CPReLU has the best performance. The rest of the results are reported by using CPReLU activation.

Fig. 6 shows the qualitative results of our final model for reconstruction of two 20% and 30% undersampled images from the MICCAI 2013 dataset. It is observed that the proposed model is able to reconstruct high-quality images by preserving most of the structural details. Also, we observe that use of noisy images during training helps in reducing the impact of noise on the reconstruction quality.

Table 3. Comparison with previous methods using MICCAI 2013 dataset

Method	Noise-free images PSNR (dB) / mSSIM	10% noise added PSNR (dB)	20% noise added PSNR (dB)
ZFR	35.61 / 0.7735	24.42	18.56
DeepADMM[41]	37.36 / 0.8534	25.19	19.33
DLMRI[32]	38.24 / 0.8020	24.52	18.85
Noislet[29]	39.01 / 0.8588	25.29	19.42
BM3D[9]	39.93 / 0.9125	24.71	18.65
DAGAN[40]	40.20 / 0.9681	37.40	34.23
Proposed	45.377 / 0.9930	41.793	39.057

Table 3 illustrates the comparison of the proposed method with the state-of-the-art approaches. These results are reported for 30% undersampled images, from the MICCAI 2013 dataset. It can be observed that there is a significant boost in both the PSNR and mSSIM values when the proposed method is compared with existing approaches.

Table 4. Comparison with previous methods using IXI dataset

Method	PSNR (dB)	mSSIM
ZFR	29.704	0.5705
FBPCNet[19]	30.103	0.6719
DLMRI[32]	37.037	0.6864
DeepADMM[41]	35.704	0.6705
DeepCascade[35]	38.667	0.7227
Proposed	38.659	0.9598

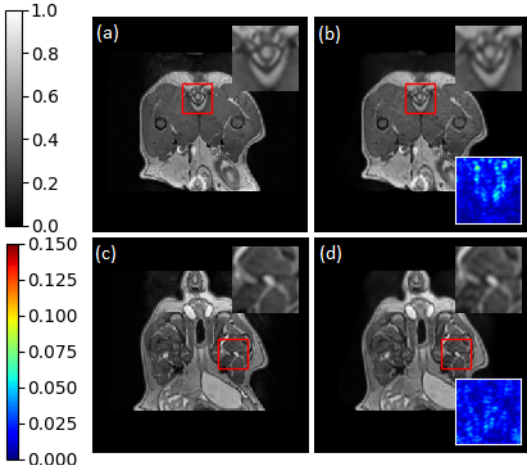


Figure 7. Results of zero-shot inference. (a), (c) GT, (b), (d) reconstruction results of the proposed model. Inset- top right: the zoomed in region enclosed by the red box, bottom right: absolute difference between the zoomed in region and its corresponding GT.

Table 4 show the comparison of the proposed method with ZFR and methods like FBPCNet [19], DeepADMM [41], DLMRI [32], and DeepCascade [35]. These results are reported for 30% undersampled images, from the IXI dataset. It can be observed that although the PSNR is marginally less, there is a significant boost in the mSSIM for the proposed method. Also, the inference step takes only 0.0227 seconds.

The model trained on 30% undersampled brain images from the MICCAI 2013 dataset is also tested for reconstruction of 30% undersampled images of canine legs from the MICCAI 2013 challenge. Fig. 7 shows the qualitative results of this zero-shot inference. The proposed model achieves an average PSNR 42.584 dB and mSSIM 0.9857, when inferred for 2000 test images.

## 4. Conclusion

In this paper, we introduced a novel complex-valued generator architecture that is trained using SSIM and wavelet losses to achieve fast yet efficient reconstruction. The fast inference step opens up the possibility for a real-time implementation of the method. Detailed analyses have shown that the proposed method significantly improves the quality of the reconstruction compared to state-of-the-art CS-MRI reconstruction methods. It has also been shown that the present model can be trained with noise based data augmentation, and it outperforms all the existing methods when reconstruction is attempted using noisy data.

## References

- [1] M. Arjovsky, S. Chintala, and L. Bottou. Wasserstein generative adversarial networks. In *Proceedings of the 34th International Conference on Machine Learning*, volume 70, pages 214–223, International Convention Centre, Sydney, Australia, 06–11 Aug 2017.
- [2] M. Arjovsky, A. Shah, and Y. Bengio. Unitary evolution recurrent neural networks. *CoRR*, abs/1511.06464, 2015.
- [3] A. Bora, A. Jalal, E. Price, and A. G. Dimakis. Compressed sensing using generative models. In *Proceedings of the 34th International Conference on Machine Learning*, volume 70, pages 537–546, 2017.
- [4] S. Boyd, N. Parikh, E. Chu, B. Peleato, and J. Eckstein. Distributed optimization and statistical learning via the alternating direction method of multipliers. *Foundations and Trends in Machine Learning*, 3(1):1–122, 2011.
- [5] I. Danihelka, G. Wayne, B. Uria, N. Kalchbrenner, and A. Graves. Associative long short-term memory. *CoRR*, abs/1602.03032, 2016.
- [6] P. Deora, B. Vasudeva, S. Bhattacharya, and P. M. Pradhan. Robust compressive sensing mri reconstruction using generative adversarial networks. *CoRR*, abs/1910.06067, 2019.
- [7] C. Dong, C. C. Loy, K. He, and X. Tang. Image super-resolution using deep convolutional networks. *IEEE Transactions on Pattern Analysis and Machine Intelligence*, 38(2):295–307, Feb. 2016.
- [8] D. L. Donoho. Compressed sensing. *IEEE Transactions on Information Theory*, 52(4):1289–1306, April 2006.
- [9] E. M. Eksioglu. Decoupled algorithm for MRI reconstruction using nonlocal block matching model: BM3D-MRI. *Journal of Mathematical Imaging and Vision*, 56(3):430–440, Nov 2016.
- [10] I. Goodfellow, J. Pouget-Abadie, M. Mirza, B. Xu, D. Warde-Farley, S. Ozair, A. Courville, and Y. Bengio. Genera-

tive adversarial nets. In *Advances in Neural Information Processing Systems 27*, pages 2672–2680. Curran Associates, Inc., 2014.

[11] M. A. Griswold, P. M. Jakob, R. M. Heidemann, M. Nittka, V. Jellus, J. Wang, B. Kiefer, and A. Haase. Generalized auto-calibrating partially parallel acquisitions (GRAPPA). *Magnetic Resonance in Medicine*, 47(6):1202–1210, 2002.

[12] N. Guberman. On complex valued convolutional neural networks. *CoRR*, abs/1602.09046, 2016.

[13] K. He, X. Zhang, S. Ren, and J. Sun. Delving deep into rectifiers: Surpassing human-level performance on imagenet classification. In *Proceedings of the 2015 IEEE International Conference on Computer Vision (ICCV)*, ICCV ’15, pages 1026–1034, Washington, DC, USA, 2015. IEEE Computer Society.

[14] A. Hirose and S. Yoshida. Generalization characteristics of complex-valued feedforward neural networks in relation to signal coherence. *IEEE Transactions on Neural Networks and learning systems*, 23(4):541–551, 2012.

[15] G. Huang, Z. Liu, L. v. d. Maaten, and K. Q. Weinberger. Densely connected convolutional networks. In *2017 IEEE Conference on Computer Vision and Pattern Recognition (CVPR)*, pages 2261–2269, July 2017.

[16] H. Huang, R. He, Z. Sun, and T. Tan. Wavelet-SRNet: A wavelet-based CNN for multi-scale face super resolution. In *2017 IEEE International Conference on Computer Vision (ICCV)*, pages 1698–1706, Oct 2017.

[17] S. Ioffe and C. Szegedy. Batch normalization: Accelerating deep network training by reducing internal covariate shift. In *Proceedings of the 32nd International Conference on International Conference on Machine Learning - Volume 37*, ICML’15, pages 448–456. JMLR.org, 2015.

[18] P. Isola, J. Zhu, T. Zhou, and A. A. Efros. Image-to-image translation with conditional adversarial networks. In *IEEE Conference on Computer Vision and Pattern Recognition (CVPR)*, pages 5967–5976, July 2017.

[19] K. H. Jin, M. T. McCann, E. Froustey, and M. Unser. Deep convolutional neural network for inverse problems in imaging. *IEEE Transactions on Image Processing*, 26(9):4509–4522, Sep. 2017.

[20] D. P. Kingma and J. Ba. Adam: A method for stochastic optimization. In *3rd International Conference on Learning Representations, ICLR 2015, San Diego, CA, USA, Conference Track Proceedings*, 2015.

[21] K. Kreutz-Delgado. The complex gradient operator and the CR-calculus. *CoRR*, abs/0906.4835, 2009.

[22] B. Landman and S. Warfield (Eds.). 2013 Diencephalon standard challenge.

[23] Y. Liu, J. F. Cai, Z. Zhan, D. Guo, J. Ye, Z. Chen, and X. Qu. Balanced sparse model for tight frames in compressed sensing magnetic resonance imaging. *PLOS ONE*, 10(4):1–19, 2015.

[24] M. Lustig, D. Donoho, and J. M. Pauly. Sparse MRI: The application of compressed sensing for rapid MR imaging. *Magnetic Resonance in Medicine*, 58(6):1182–1195, 2007.

[25] M. Mardani, E. Gong, J. Y. Cheng, S. S. Vasanawala, G. Zarchuck, L. Xing, and J. M. Pauly. Deep generative adversarial neural networks for compressive sensing mri. *IEEE Transactions on Medical Imaging*, 38(1):167–179, Jan 2019.

[26] M. Mirza and S. Osindero. Conditional generative adversarial nets. *ArXiv*, abs/1411.1784, 2014.

[27] T. Nitta. On the critical points of the complex-valued neural network. In *Proceedings of the 9th International Conference on Neural Information Processing, 2002. ICONIP ’02.*, volume 3, pages 1099–1103 vol.3, Nov 2002.

[28] A. V. Oppenheim and J. S. Lim. The importance of phase in signals. *Proceedings of the IEEE*, 69(5):529–541, 1981.

[29] K. Pawar, G. Egan, and J. Zhang. Multichannel compressive sensing MRI using noiselet encoding. *PLOS ONE*, 10(5):1–27, 2015.

[30] K. P. Pruessmann, M. Weiger, M. B. Scheidegger, and P. Boesiger. SENSE: Sensitivity encoding for fast MRI. *Magnetic Resonance in Medicine*, 42(5):952–962, 1999.

[31] T. M. Quan, T. Nguyen-Duc, and W. Jeong. Compressed sensing mri reconstruction using a generative adversarial network with a cyclic loss. *IEEE Transactions on Medical Imaging*, 37(6):1488–1497, June 2018.

[32] S. Ravishankar and Y. Bresler. MR image reconstruction from highly undersampled k-space data by dictionary learning. *IEEE Transactions on Medical Imaging*, 30(5):1028–1041, May 2011.

[33] D. P. Reichert and T. Serre. Neuronal synchrony in complex-valued deep networks. *CoRR*, abs/1312.6115, 2013.

[34] O. Ronneberger, P. Fischer, and T. Brox. U-net: Convolutional networks for biomedical image segmentation. In *International Conference on Medical image computing and computer-assisted intervention*, pages 234–241. Springer, 2015.

[35] J. Schlemper, J. Caballero, J. V. Hajnal, A. N. Price, and D. Rueckert. A deep cascade of convolutional neural networks for dynamic MR image reconstruction. *IEEE Transactions on Medical Imaging*, 37(2):491–503, Feb 2018.

[36] C. Trabelsi, O. Bilaniuk, Y. Zhang, D. Serdyuk, S. Subramanian, J. F. Santos, S. Mehri, N. Rostamzadeh, Y. Bengio, and C. J. Pal. Deep complex networks. In *6th International Conference on Learning Representations, ICLR 2018, Vancouver, BC, Canada, April 30 - May 3, 2018, Conference Track Proceedings*, 2018.

[37] X. Wang, K. Yu, S. Wu, J. Gu, Y. Liu, C. Dong, Y. Qiao, and C. C. Loy. Esrgan: Enhanced super-resolution generative adversarial networks. In *The European Conference on Computer Vision (ECCV) Workshops*, pages 63–79, September 2018.

[38] S. Wisdom, T. Powers, J. Hershey, J. Le Roux, and L. Atlass. Full-capacity unitary recurrent neural networks. In *Advances in Neural Information Processing Systems*, pages 4880–4888, 2016.

[39] J. Xie, L. Xu, and E. Chen. Image denoising and inpainting with deep neural networks. In *Advances in Neural Information Processing Systems 25*, pages 341–349. Curran Associates, Inc., 2012.

[40] G. Yang, S. Yu, H. Dong, G. Slabaugh, P. L. Dragotti, X. Ye, F. Liu, S. Arridge, J. Keegan, Y. Guo, and D. Firmin. DAGAN: Deep de-aliasing generative adversarial networks for

fast compressed sensing MRI reconstruction. *IEEE Transactions on Medical Imaging*, 37(6):1310–1321, June 2018.

[41] Y. Yang, J. Sun, H. Li, and Z. Xu. Deep ADMM-Net for compressive sensing MRI. In *Advances in Neural Information Processing Systems 29*, pages 10–18. Curran Associates, Inc., 2016.

[42] Z. Wang, A. C. Bovik, H. R. Sheikh, and E. P. Simoncelli. Image quality assessment: From error visibility to structural similarity. *IEEE Transactions on Image Processing*, 13(4):600–612, April 2004.